

Evidence of Chaotic Pattern in Solar Flux Through a Reproducible Sequence of Period-Doubling-Type Bifurcations

S. Ashrafi and L. Roszman
COMPUTER SCIENCES CORPORATION (CSC)

ABSTRACT

This paper presents a preliminary study of the limits to solar flux intensity prediction, and of whether the general lack of predictability in the solar flux arises from the nonlinear chaotic nature of the Sun's physical activity. Statistical analysis of a chaotic signal can extract only its most gross features, and detailed physical models fail, since even the simplest equations of motion for a nonlinear system can exhibit chaotic behavior.

A recent theory by Feigenbaum suggests that nonlinear systems that can be led into chaotic behavior through a sequence of period-doubling bifurcations will exhibit a universal behavior. As the control parameter is increased, the bifurcation points occur in such a way that a proper ratio of these will approach the universal Feigenbaum number. Experimental evidence supporting the applicability of the Feigenbaum scenario to solar flux data is sparse. However, given the hypothesis that the Sun's convection zones are similar to a Rayleigh-Benard mechanism, we can learn a great deal from the remarkable agreement observed between the prediction by theory (period doubling — a universal route to chaos) and the amplitude decrease of the signal's regular subharmonics.

This paper will show that period-doubling-type bifurcation is a possible route to a chaotic pattern of solar flux that is distinguishable from the logarithm of its power spectral density. This conclusion is the first positive step toward a reformulation of solar flux by a nonlinear chaotic approach.

The ultimate goal of this research is to be able to predict an estimate of the upper and lower bounds for solar flux within its predictable zones. Naturally, it is an important task to identify the time horizons beyond which predictability becomes incompatible with computability.

1. INTRODUCTION

An accurate forecast of the intensity of solar flux is a prerequisite to accurate orbit and lifetime prediction for spacecraft. The orbit lifetime is a function of the atmospheric drag force. The drag depends on the atmospheric density, which is influenced by the solar flux. Solar ultraviolet and X-ray emissions that directly affect the Earth's atmosphere are highly correlated with solar flux F10.7 observed on the surface of the Earth. Present density models, such as Jacchia-Roberts (J-R), Harris-Priester (H-P), and mass spectrometer incoherent scatter (MSIS), use F10.7 solar flux intensity as the indicator of the potential strength of ionizing radiation (References 1, 2, 3, and 4).

Current forecasting methods use statistical models to predict solar flux; for example, the Schatten method used by Goddard Space Flight Center (GSFC), Marshall Space Flight Center (MSFC), and National Oceanic and Atmospheric Administration (NOAA) (Reference 5). These models use traditional stochastic analysis (usually based on structurally random data) to predict solar flux. However, as shown below, the patterns exhibited by the solar flux data indicate that the dynamical system creating the solar flux signal is inherently chaotic rather than completely stochastic. Starting with the postulate that solar flux is a chaotic time series, a chaotic model is developed to reproduce essential features of the solar flux signal.

The solar flux signal is classified in Section 2 through analysis of a few basic descriptive properties. Section 3 presents a possible model for the solar flux signal based upon recently developed nonlinear dynamics concepts of period-doubling bifurcations and upon the results shown in References 5, 6, 7, and 8.

2. CLASSIFICATION OF SOLAR FLUX SIGNAL

Signals such as the solar flux have been categorized historically as either deterministic (meaning that a model of the physical system can be constructed and used to predict the particular signal that will occur at a given time from a signal(s) at a another time) or random (meaning that no model of the physical system can be constructed, but, rather, that a method can be found to predict the probability that any particular signal will occur at a given time, based on the history of the signal). These general categories can be divided further, as shown in Figure 1. For deterministic signals, predictability is achieved by deriving for the model of the system equations of motion for the signal. For random signals, a statistical analysis of the signal history must be performed and either an existing statistical theory applied or a new statistical theory constructed.

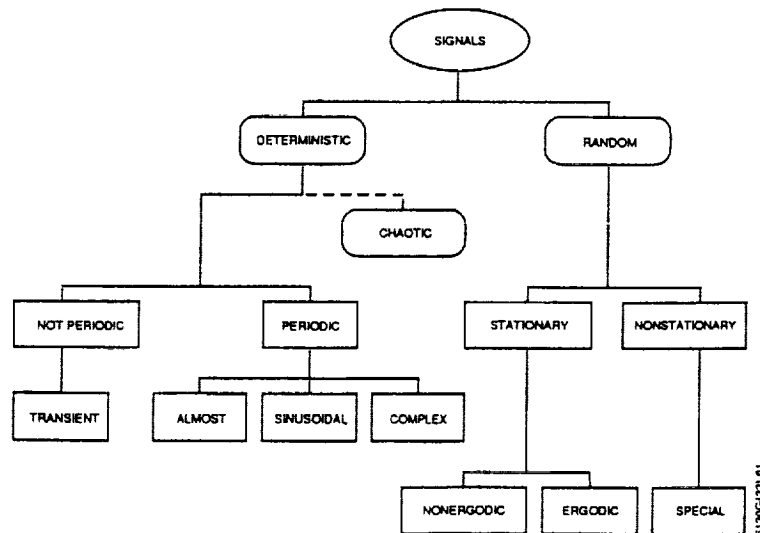


Figure 1. Categories of Signals in Data Analysis

Recent research on dynamic systems indicates that the cascade of categorizations shown in Figure 1 is incomplete and that signals can exist for a system that has a detailed physical model (the system is deterministic), but that the derived equations of motion cannot be used to predict the signal. Such signals and their systems of origin are categorized as chaotic. While the lack of predictability in a deterministic system may seem inconsistent, mathematical precision must be separated from the precision of physical observation. When a model is mathematically deterministic, only one solution to its equations of motion exists for the given initial conditions (Reference 9). To predict a signal to some specified accuracy, the observer must know the initial conditions of the system to some related accuracy; however, one well-defined class of models has equations of motion for which variations beyond the precision of the observer's knowledge of the initial conditions prevent predictions to a specified accuracy. Terrestrial weather (to which solar activity is perfectly analogous) is an example of such a chaotic system.

Several statistical functions can be used to analyze the possible extent of the chaotic nature of the solar flux signal. Sections 2.1 and 2.2 present the application of these functions, and Section 2.3 presents some conclusions.

2.1 AUTOCOVARANCE AND AUTOCORRELATION OF THE SOLAR FLUX

The solar flux data shown in Figure 2 present an example of a statistical time series. By plotting a scatter diagram using pairs of values (f_t, f_{t+l}) of a time series, we can visualize the joint probability distribution $P(f_i, f_j)$. For the solar flux data from Figure 2(a), we obtain the scatter diagram in Figure 3 for lags of $l = 0$ and $l = 27$. By plotting f_{t+27} versus f_t (Reference 10), this plot shows that the correlation between f_{t+27} and f_t is positive.

Figure 4 shows the plots of autocovariances, autocorrelations, and autocorrelation errors for 600 shifts. These plots were generated from more than 4,000 points of the solar flux time series shown in Figure 2(b).

Figures 5(a) and 5(b) show the plots of the power spectra for the solar flux data from Figures 2(a) and 2(b), respectively. Figure 6 has the plot of the power spectra of data from Figure 2(a), scaled to have the same horizontal axis as in Figure 5(b). This plot was scaled to show a global symmetry of the power spectra under time extension.

2.2 FOURIER FILTERING

In the low-pass Fourier filter method, we Fourier-transform the signal and then take the inverse Fourier-transform, omitting frequencies greater than a specified limit. Using this technique, we can determine what frequencies to disregard for construction of a simple iterative map. Figure 7 contains the solar flux time series for the period November 1977 to November 1980, and a plot for 27-point rectangular averaging. Figure 8 has plots from 7- and 27-point triangular averaging. Figure 9 shows a plot of Fourier-filtered solar flux time series with 20 and 50 harmonics retained.

2.3 CONCLUSIONS FROM STATISTICAL ANALYSIS

Looking at the solar flux time series shown in Figure 2(a), it is difficult to see any pattern or structure in the solar flux data. However, the scatter diagram of Figure 3(b) shows regions where points are clustered together. This clustering is an indication of correlation between f_t and f_{t+27} . Figure 4 has a plot of the autocovariance and autocorrelation function with its standard error, and shows the small peaks that are separated by exactly 27-day solar rotations. Additionally, we can see that every 183 days, an anomaly occurs in the autocorrelation function. This anomaly is probably due to a change of the magnetic latitude of the Earth every 6 months ($\frac{1}{2}$ year \approx 183 days). To determine if this is a numerical or computational artifact, we also have plotted the standard error of autocorrelation function. At the particular location of these anomalies, no considerable change in standard error of autocorrelation function was observed; therefore, these anomalies are dynamical in character and are not produced by computational artifacts. The autocorrelation plots show that the autocorrelation of the solar flux decreases with increasing time shifts, a characteristic common to chaotic time series.

Comparing Figure 8(a) to Figure 9(b), and Figure 8(b) to Figure 9(c), we can see that 27-point triangular averaging is equivalent to retaining 20 harmonics in a Fourier low-pass filtered solar flux signal; 7-point triangular averaging is equivalent to retaining 50 harmonics. This information is useful for constructing an iterative

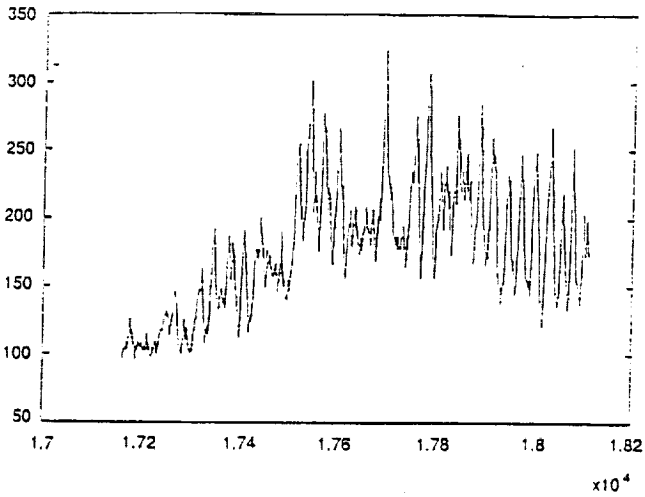


Figure 2(a). Short-Duration Solar Flux F10.7 (10^{-22} watt/m².Hz) Plotted Versus Modified Julian Date (MJD)

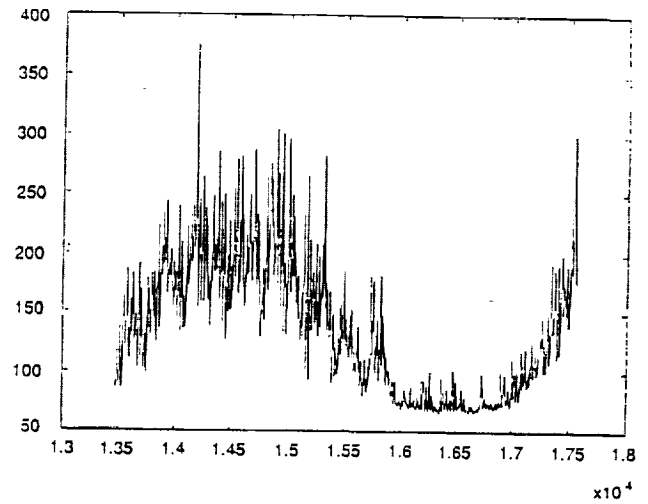


Figure 2(b). Long-Duration Solar Flux F10.7 Plotted Versus Modified Julian Date (MJD)

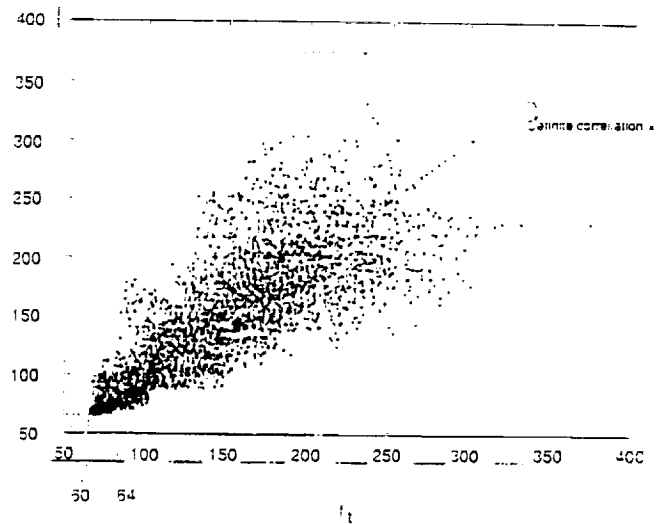
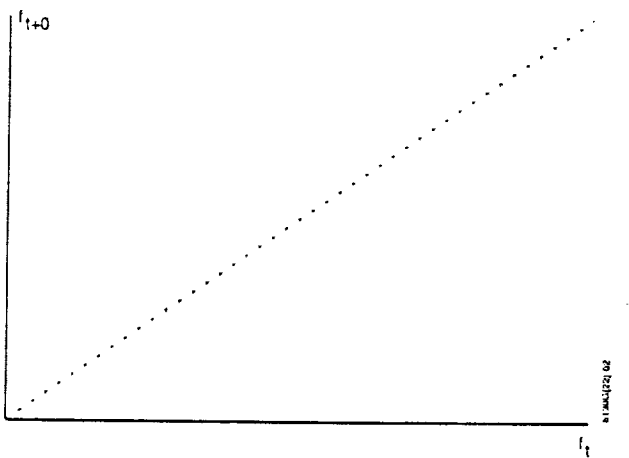
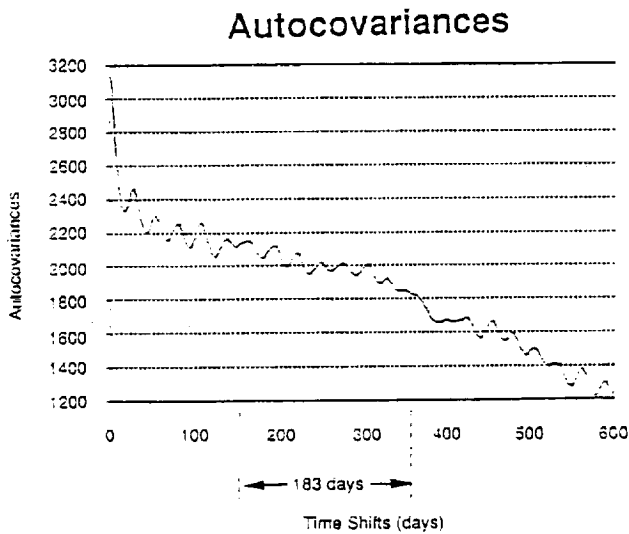


Figure 3. Scatter Diagram at Lags (a) $\ell = 0$ and (b) $\ell = 27$



A time series could be checked to determine whether θ_k is zero after a lag l . A check is necessary to identify a model for a time series. The approximate form of the variance of the estimated autocorrelation coefficient is given by

$$\text{var}[r_l] = \frac{1}{n} \sum_{j=-\infty}^{\infty} (e_j^2 + e_{j+l}e_{j-l} - 2e_j e_{j+l} + 2e_l^2 e_j^2)$$

If autocorrelation damps out exponentially ($e_l = \psi^{|l|}$, $(-1 < \psi < 1)$), then

$$\text{var}[r_l] = \frac{1}{n} \left[\frac{(1 + \psi^2)(1 - \psi^{2l})}{1 - \psi^2} - 2l\psi^{2l} \right]$$

Figure 4(a). Plot of Autocovariances for Solar Flux Time Series of Figure 2(b) (600 Shifts)

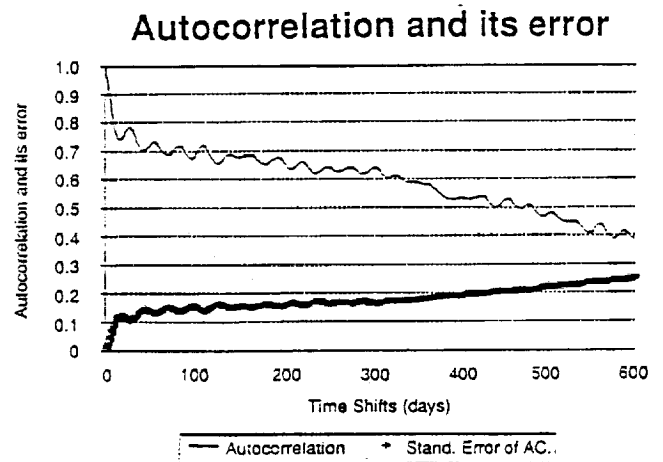


Figure 4(b). Plot of Autocorrelation and Standard Error of Autocorrelation for Solar Flux Time Series of Figure 2(b) (600 Shifts)

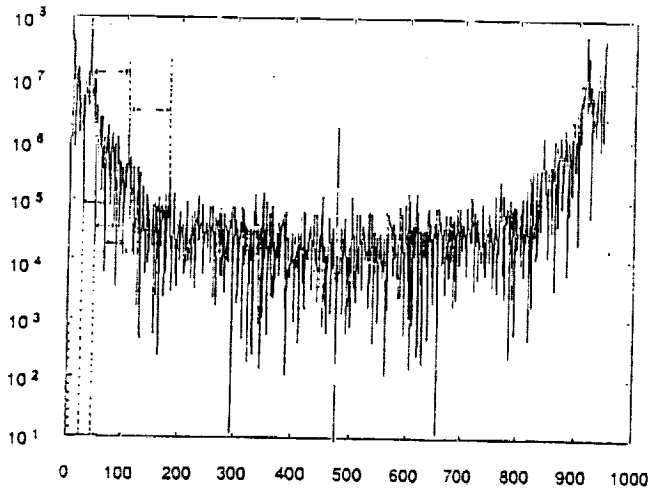


Figure 5(a). Logarithm of Power Spectrum for Solar Flux Time Series of Figure 2(a)

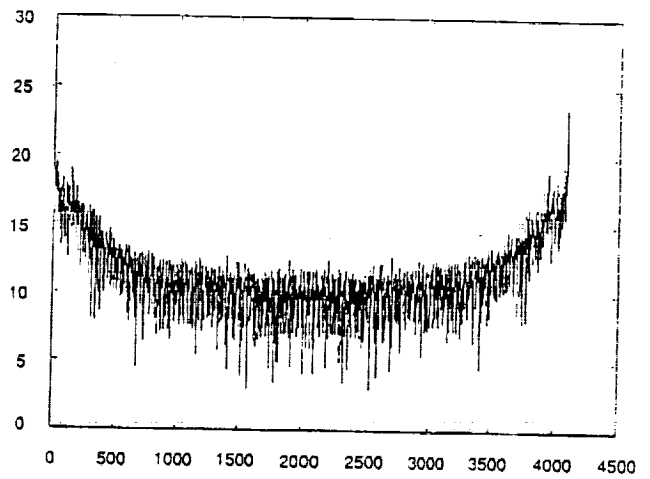


Figure 5(b). Logarithm of Power Spectrum for Solar Flux Time Series of Figure 2(b)

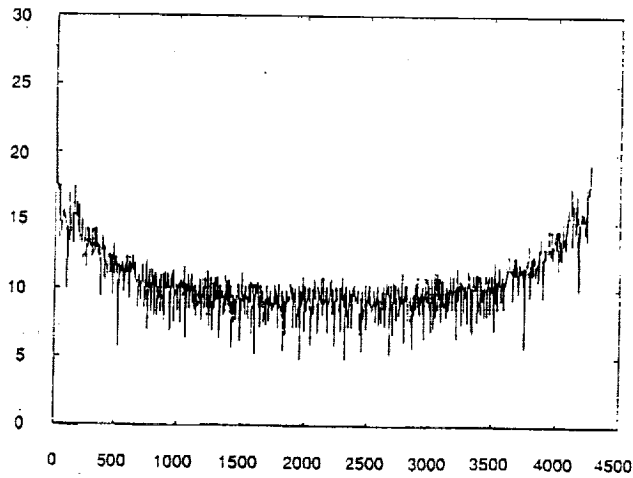


Figure 6. Logarithm of Power Spectrum for Solar Flux Time Series of Figure 2(a), Scaled to the Timespan of Figure 2(b)

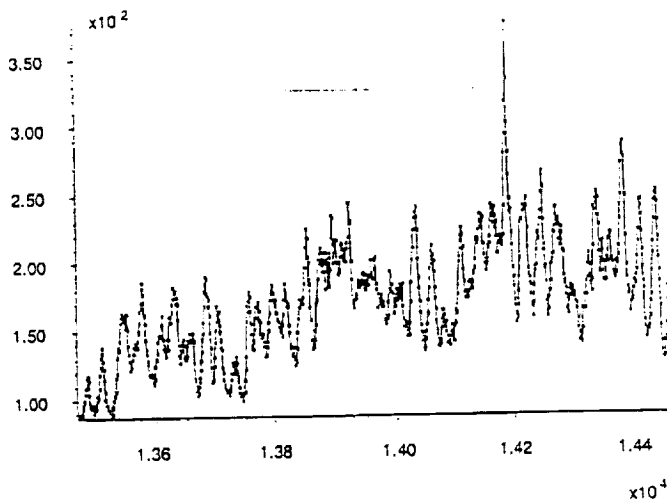
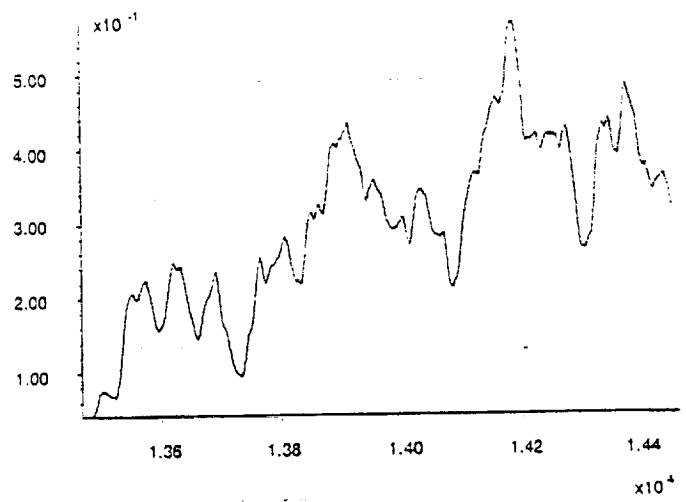


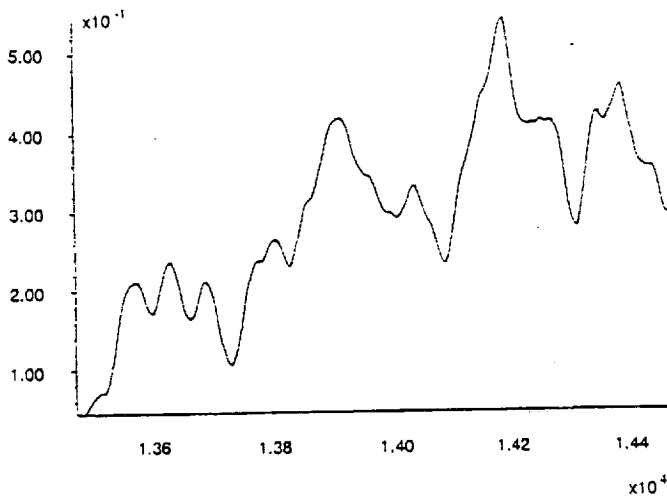
Figure 7(a). Solar Flux Time Series Versus Modified Julian Dates; The Dots Indicate Solar Flux Values Measured at That Specific Day



$$\bar{f}_i = \frac{f_{i-3} + f_{i-2} + f_{i-1} + f_i + f_{i+1} + f_{i+2} + f_{i+3}}{7}$$

for $i = 4$ to 7

Figure 7(b). 27-Point Rectangular Average From Figure 7(a)



$$\bar{f}_i = \frac{f_{i-3} + 2f_{i-2} + 3f_{i-1} + 4f_i + 3f_{i+1} + 2f_{i+2} + f_{i+3}}{16}$$

for $i = 4$ to 7

Figure 8(a). 27-Point Triangular Average of Solar Flux Time Series of Figure 7(a)

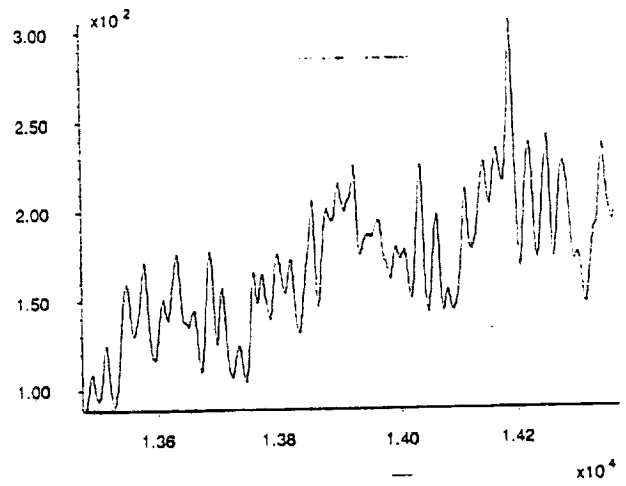


Figure 8(b). 7-Point Triangular Average of Solar Flux Time Series of Figure 7(a)

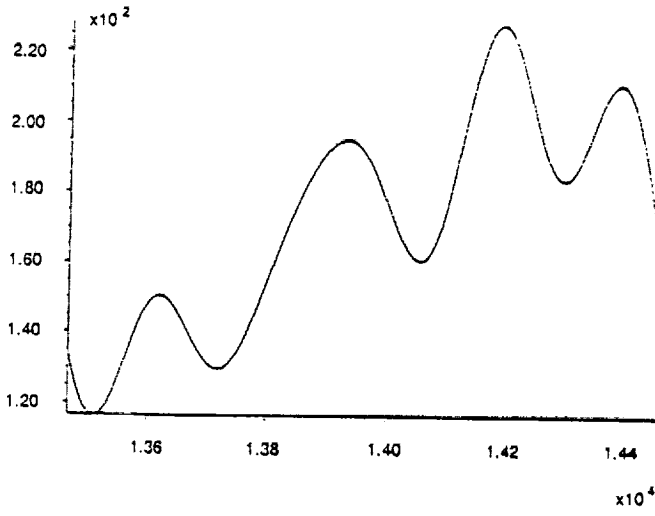


Figure 9(a). Fourier-Filtered (5 Harmonics Retained) Signal From Solar Flux Time Series of Figure 7(a)

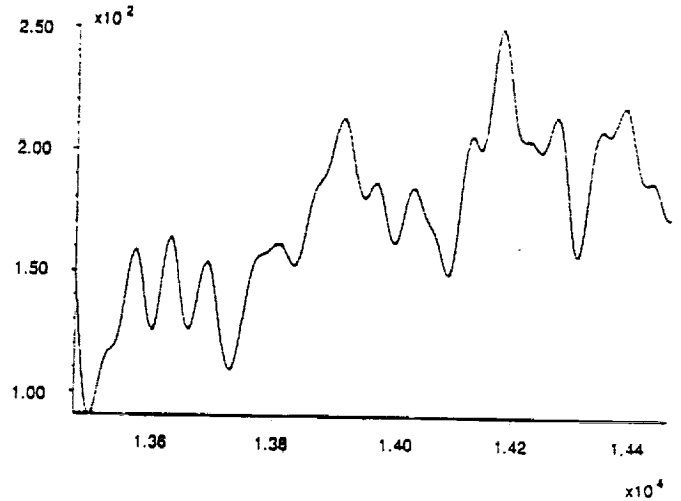


Figure 9(b). Fourier-Filtered (20 Harmonics Retained) Signal From Solar Flux Time Series of Figure 7(a)

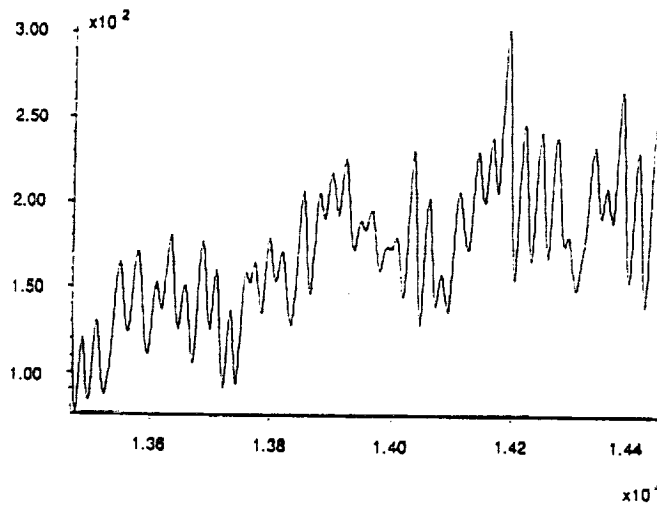


Figure 9(c). Fourier-Filtered (50 Harmonics Retained) Signal From Solar Flux Time Series of Figure 7(a)

manifold (see Section 3) that can reproduce our time series. Figure 10 shows the Fourier spectrum of the autocorrelation of the time series shown in Figure 8(a), which clearly shows the particular patterns such as the 27-day periodicity, the 183-day anomaly, and other periodic anomalies.

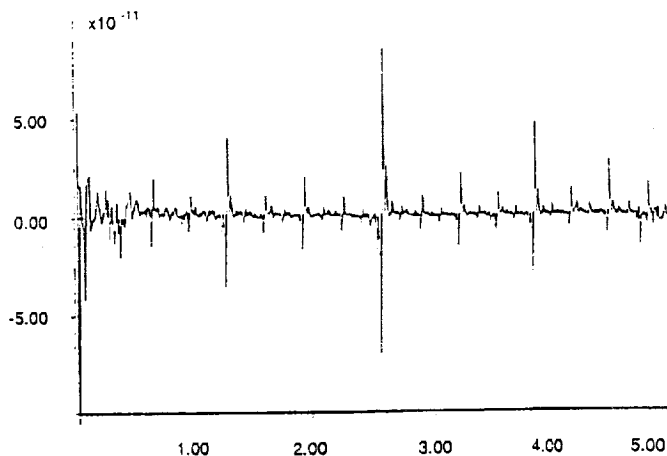


Figure 10. Fourier-Transform of the Autocorrelation of the Solar Flux Time Series From Figure 7(a), Showing the Periodicity Pattern in the Autocorrelation Function

Figure 6 shows the plot of a power spectrum for a timespan that was scaled for another time space. This plot was done to observe the global symmetry of the power spectra under time extension (a fractal characteristic). Fractal structures are common to chaotic time series.

Figures 5(a) and 5(b) show the plots of the power spectra for the solar flux data presented in Figures 2(a) and 2(b), respectively. Many obvious patterns are evident in the power spectra of Figure 5(a); for example, we can clearly see the peaks for 27-day solar rotation periodicity. One interesting feature of this figure is that, starting from the midpoint of the spectra (the "glitch" close to the 480 Fourier component), we can find the first largest glitch to the left at about the 295 Fourier component. If we divide the distance from 295 to 480 by 2, we see the next-largest downward glitch near the 390 Fourier component. Furthermore, if we divide the distance from the 295 glitch to the 390 glitch, we will once again find the next-largest glitch. The regular appearance of these glitches demonstrates successive frequency halving or period doubling for the solar flux signal. In laboratory experiments, period doubling was observed in several chaotic systems (Reference 11). As with the solar flux signal, noise limited the number of observed period doublings to only a few. Based upon laboratory experiments, we conclude that period doubling is a possible route to chaos in the solar flux signal. (Currently, three established routes to chaos have been found: the Grossmann-Feigenbaum period-doubling route, the Manneville-Pomeau route, and the Ruelle-Takens-Newhouse route.)

3. INTRODUCTION TO CHAOS IN DYNAMICAL SYSTEMS

This section presents some examples of the various states of chaos.

3.1 EXAMPLES OF CHAOTIC SYSTEMS

Two examples are introduced here. The first one (Rayleigh-Benard) is very similar to the dynamical behavior of the Sun. The second one (dripping faucet) is a model system for studying the strange attractor of solar flux; because it exhibits period doubling, it is a good candidate for studying solar flux.

Most scientists know the dynamical behavior of systems in which systems eventually settle into either periodic motion (limit cycle) or into a steady state (system ceases its motion). However, another important class is called the chaotic system. This system cannot be represented using standard analytical functions (Reference 12).

Our first example considers the dripping faucet model (see Figures 11, 12, 13, and 14). In this model, water drops fall from the faucet at a steady rate, the drops pass a detector, and the pattern is seen to be periodic. When the rate of flow is small, the time difference between the drops ($\Delta t = t_{i+1} - t_i$) is constant. As the rate is increased, two drops fall together over a longer period. Therefore, two periods are associated with this system: one is short, Δt_S , and the other is long, Δt_L . The sequence of time intervals, then, is $\dots \Delta t_S, \Delta t_L, \Delta t_S, \Delta t_L$. This interval is called period-two sequence. Longer periodic sequences are possible at a specific flow rate. This sequence can become irregular and therefore chaotic (Reference 13).

Our second example considers the experiment of Libchaber and Maurer (Reference 11). In this experiment, a liquid contained in a small box is heated from the bottom. The important points are as follows:

- The experiment has a controllable parameter, the Rayleigh number, which is proportional to the temperature difference between the bottom and the top of the cell. The Rayleigh number describes the stability of a convective flow.
- The system is dissipative. Whenever the Rayleigh number is increased, the transients begin to die out. For small temperature gradients, heat flows across the cell, but the liquid is static. At a critical temperature, a convective flow sets in. The hot liquid rises in the middle, the cool liquid flows down at the sides, and the two convective rolls appear (see Figure 15).

As the temperature difference is increased further, the rolls become unstable in a very specific way—a wave starts running along the roll, as shown in Figure 16(a). As the warm liquid rises on one side of the roll and cool liquid descends down the other side, the position and the sideways velocity of the ridge can be measured with a thermometer, as shown in Figure 16(b). A sinusoid is then observed, as shown in Figure 17(a); two other ways of displaying the measurement are suggested by the graphs in Figure 17(b).

The temperature difference is now increased. After the stabilization of the phase-space trajectory, a new wave is observed superimposed on the original sinusoidal instability. The three ways of looking at it (real time, phase-space, and frequency spectrum) are illustrated in Figure 18.

At first it appears that T_0 is the periodicity; however, a closer look reveals that the phase-space trajectory misses the starting point at T_0 and closes on itself only after $2T_0$. A new band has appeared at half the original frequency on the frequency spectrum. Its amplitude is small because the phase-space trajectory is still approximately a circle with periodicity T_0 .

As the temperature increases slightly, a fascinating thing happens. The phase-space trajectory undergoes the very fine splitting seen in Figure 19(a).

Three scales are involved here: casual observation reveals a circle with period T_0 ; closer scrutiny shows \heartsuit with period $2T_0$; and very close examination shows that the trajectory closes on itself only after $4T_0$. The same information can be read off the frequency spectrum; the dominant frequency is f_0 (the circle), then $f_0/2$, and finally, much weaker $f_0/4$ and $3f_0/4$.

The experiment now becomes very difficult. A tiny increase in the temperature gradient causes the phase-space trajectory to split on an even finer scale, with the periodicity 2^3T_0 . If the noise were not too loud to continue, it would be expected that these splittings would continue, yielding a trajectory with finer and finer detail and the frequency spectrum seen in Figure 19(b) with families of weaker frequency components. For a critical value of the Rayleigh number, the periodicity of the system is $2^n T_0$, and the convective rolls have become turbulent. The ripples that are running along them show no periodicity, and the spectrum of an idealized noise-free experiment contains infinitely many subharmonics. If increases are made to the temperature gradient beyond this critical value, further surprises occur. The following section provides a numerical simulation of a simple nonlinear oscillator to provide an understanding of why the phase-space trajectory splits in this peculiar fashion.

In an externally driven pendulum, one can see that for a wide range of initial points, the phase-space trajectory converges to a limit cycle (trajectory loops onto itself), which for some $k = k_0$ is as shown in Figure 20(a). If not for the external driving force, the oscillator would have simply come to a stop; as it is, it is executing a motion

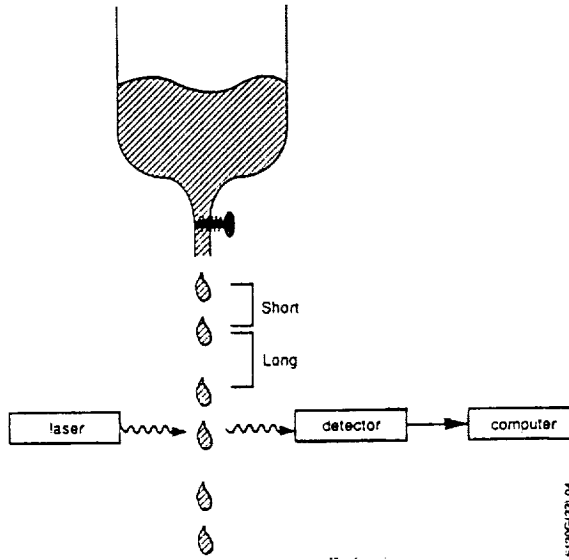


Figure 11. Dripping Faucet Experiment

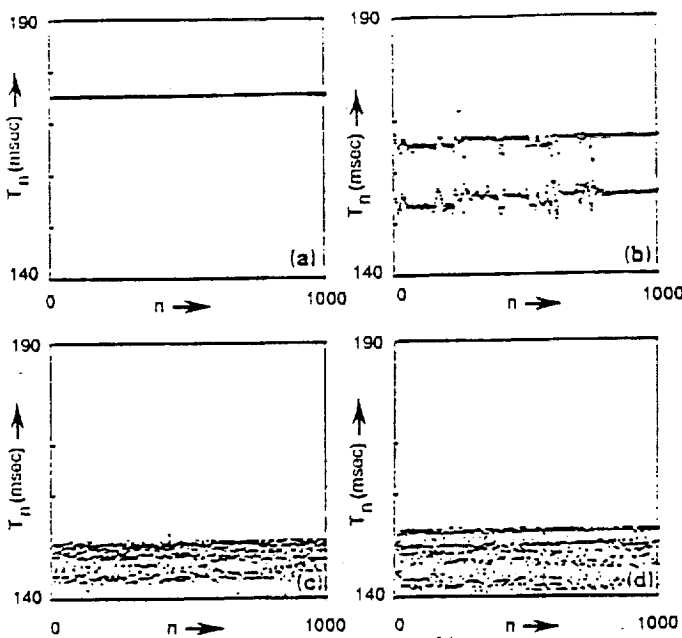


Figure 12. Time Interval Versus Drop Number at Four Low Drip Rates (Reference 10): (a) Periodic Dripping, (b) Biperiodic Dripping, (c) Chaos With an Average Interval, and (d) Chaos With a Different Average Interval

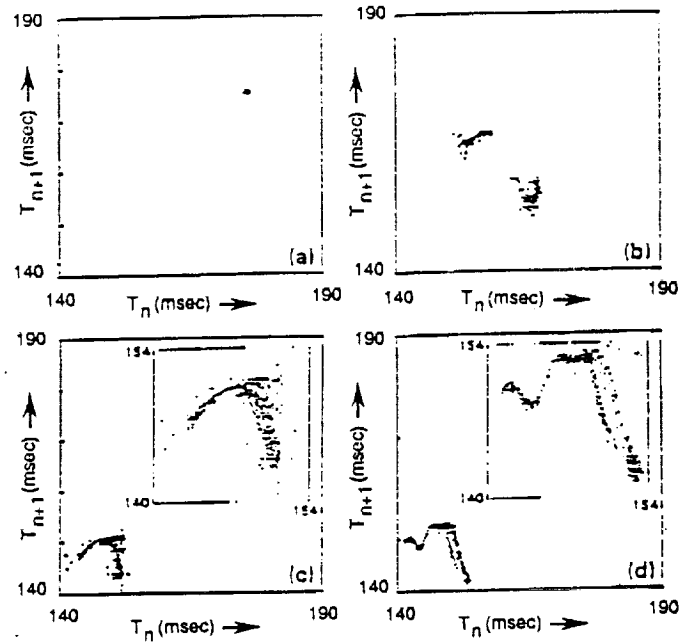


Figure 13. Time Interval Versus Next Time Interval, (T_n, T_{n+1}) , From Data of Figure 12: (a) Periodic Case, (b) Biperiodic Case, (c) The "Parabola" Formed by the Random-Looking Data of Figure 12(c), and (d) The "Camel" Formed by the Random-Looking Data of Figure 12(d)

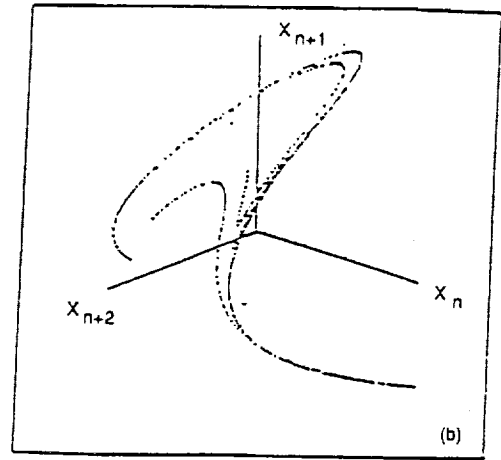
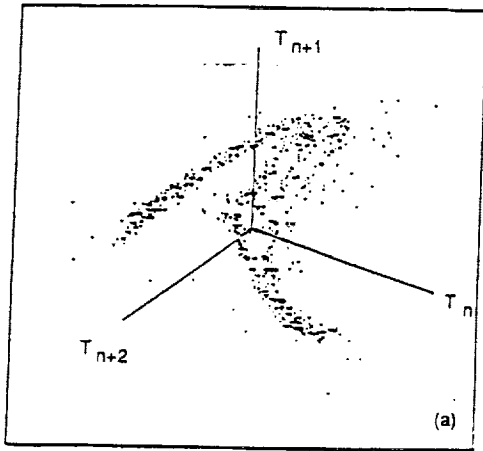


Figure 14. Sample Plots: (a) 3-Dimensional Plot (T_n, T_{n+1}, T_{n+2}) From Data of Figure 12(c), (b) The Hénon Attractor Displayed in the Same 3-Dimensional Coordinates as the Water Drop Data of Figure 14(a).

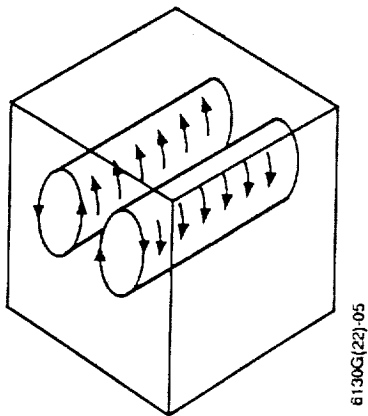
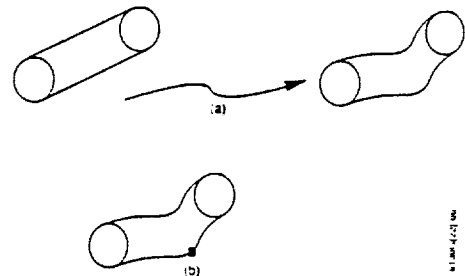
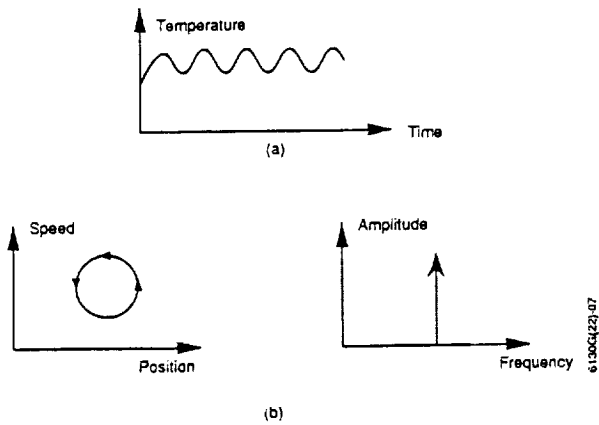


Figure 15. Rayleigh-Benard Convection Rolls



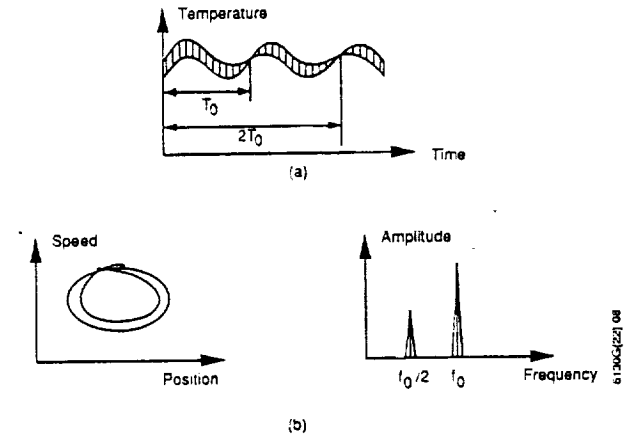
(a) A Wave Starts Running Along the Roll as the Temperature is Increased.
 (b) The Position and the Sideways Velocity of the Ridge can be measured With a Thermometer

Figure 16. Convection Rolls Affected by Temperature



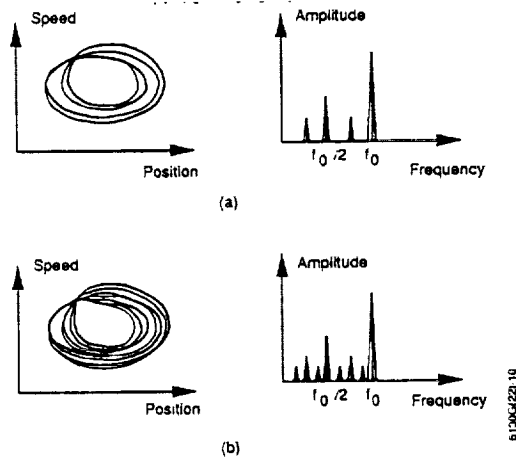
(a) Thermometer Reading, Indicating Position and Sideways Velocity of the Ridge.
 (b) Two Different Representations of This Dynamical System: Phase-Space and Frequency Representations

Figure 17. Additional Ways to Display the Measurements



(a) Time domain representation.
 (b) Phase space and frequency representation.

Figure 18. Phases-Space Trajectory Misses the Starting Point at T_0 and Closes on Itself Only After $2T_0$



(a) As the Temperature Gradient is Increased, the Phase-Space Trajectory Undergoes a Very Fine Splitting: Phase-Space and Frequency Representations.
 (b) A Tiny Increase in the Temperature Gradient Causes the Phase-space Trajectory to Split on an Even Finer Scale with Periodicity $2^3 T_0$.

Figure 19. Phase-Space Trajectories

forced on it externally, independent of the initial displacement and velocity. It is easy to visualize this nonlinear pendulum executing little backward jerks as it swings back and forth. Starting at the point marked 1, the pendulum returns to it after the unit period T_0 . However, as the friction is decreased, the same phenomenon is observed as in the turbulence experiment where the limit cycle undergoes a series of period doubling as illustrated in Figure 20(b).

The trajectory continues to nearly miss the starting point, until it hits after $2^n T_0$. The phase-space trajectory is getting increasingly hard to draw. However, the sequence of points 1, 2, ..., 2^n , which corresponds to the state of the oscillator at times $T_0, 2T_0, \dots, 2^n T_0$, sits in a small region of the phase space, and it can be enlarged for a closer look, as seen in Figure 21(a). Globally, the phase-space trajectories of the turbulence experiment and of the nonlinear oscillator numerical experiment look very different. However, the sequence of near misses is local and looks roughly the same for both systems, as illustrated in Figure 21(b). This method of reducing the dimensionality of the phase-space is often called a Poincaré map. Instead of starting at the entire phase-space trajectory, we find its points of intersection with a given surface. The Poincaré map contains all the needed information and enables the scientist to read off where an instability occurs and how large it is. By continuously varying the nonlinearity parameter (such as friction and Rayleigh number) and plotting the location of the intersection points (in the present case, the Poincaré surface is a line), the result is the bifurcation tree seen in Figure 22(b). A computer-generated example of a real bifurcation tree for a simple chaotic system is shown in Figure 22(a). The phase-space trajectories that have been drawn are localized so the tree has a finite span. Bifurcation occurs simultaneously because it is cutting a single trajectory; when it splits, it does so everywhere along its length. Finer and finer scales characterize both the branch separations and the branch lengths.

Feigenbaum's discovery consists of the following quantitative observations:

- The parameter convergence is universal (independent of the particular physical system), as shown in Figure 22(c).
- The relative scale of successive branch splittings is universal (independent of the particular physical system), as seen in Figure 22(d).

The beauty of this discovery is that if turbulence (chaos) is arrived at through an infinite sequence of bifurcations, the following two predictions result:

$$\delta = \lim_{i \rightarrow \text{large}} \frac{\Delta_i}{\Delta_{i+1}} = 4.6692 \qquad \alpha = \lim_{i \rightarrow \text{large}} \frac{\epsilon_i}{\epsilon_{i+1}} = 2.5029$$

3.2 SENSITIVITY TO INITIAL CONDITIONS (ATTRACTORS)

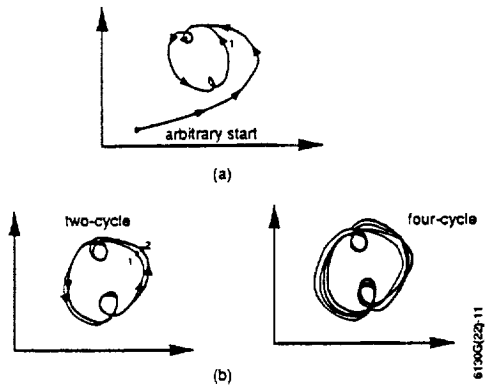
Here we intend to show that a time horizon exists above which predictions are impossible. To demonstrate this, we use the dripping faucet attractor (the Hénon attractor), which contains multiple periodicities in its dynamics.

One of the most important concepts in dynamics of dissipative systems is the presence of attracting sets, or attractors, in phase space. These are bounded sets where regions of initial conditions asymptote as time increases; that is, dynamical systems that are conservative do not have attractors. Two examples of attractors are shown in Figure 23 (Reference 14).

NOTE: The dimensionality of a point attractor is 0 and the dimensionality of a limit-cycle attractor is 1 (it is a line rather than a point). In general, the dimension of an attractor can be a noninteger fraction or a fractal attractor; such attractors are called strange attractors. An example of a strange attractor is shown in Figure 24 and is generated from the Hénon map (10^4 successive iterations).

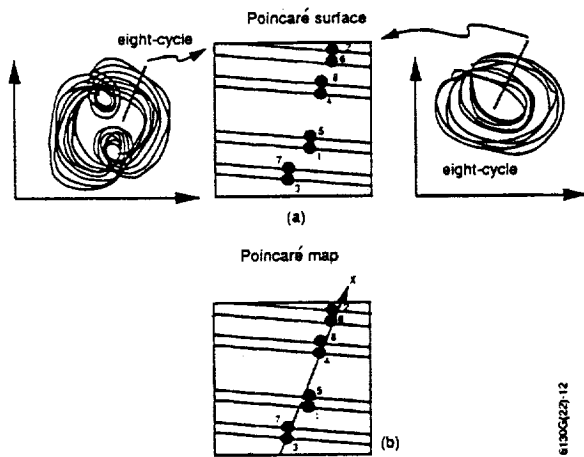
$$\begin{aligned} x_{n+1} &= A - x_n^2 + B y_n \\ y_{n+1} &= x_n \end{aligned}$$

After a small number of iterates of two trajectories, one computed using single precision, the other computed using double precision, and both originating from the same initial condition, they are still far apart. This approach was recently proposed by C. Grebogi.



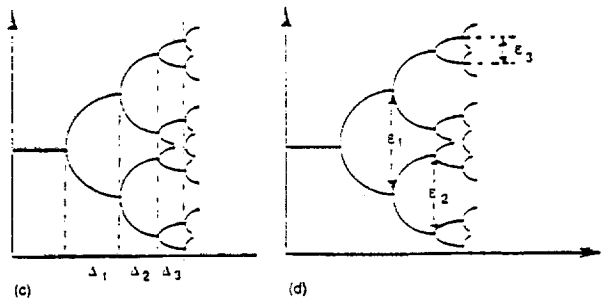
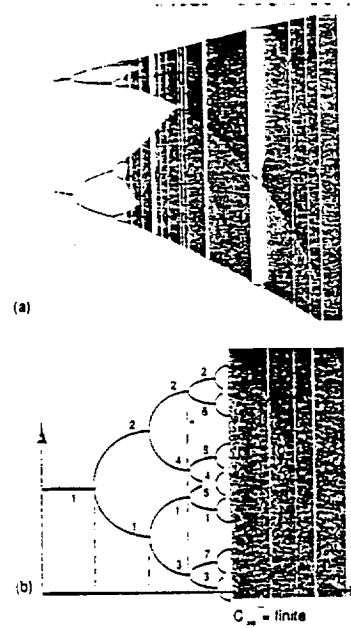
- (a) The Phase-Space Trajectory Converges to a Limit Cycle
- (b) In a Pendulum, Starting at the Point Marked 1, the Pendulum Returns to it After the Unit Period To. However as the friction is decreased, the Same Phenomenon is Observed as in the Turbulence Experiment Where the Limit Cycle Undergoes a Series of Period-Doublings

Figure 20. Phase-Space Phenomena



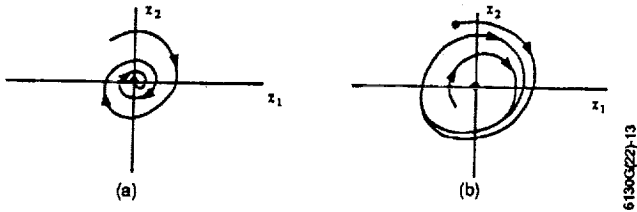
- (a) The Trajectory Continues to Nearly Miss the Starting Point Until it Hits After 2^n To Here We Have Two Different Dynamical Systems: a Pendulum and a Rayleigh-Bernard System, but They are Both Led to Chaotic Behavior Through the Same Universal Route (Period-Doublings). The Poincaré Surface Reveals This Universality.
- (b) The Segments of Near Misses is Local and Looks Roughly the Same for Both the Pendulum System and the Rayleigh-Bernard System.

Figure 21. Comparison of Trajectory Systems



- (a) Computer-Generated version of a Real Bifurcation for a Chaotic System.
- (b) Location of Intersection Points in the Present Mechanisms: the Poincaré Surface is a Line and the Result is a Bifurcation Tree.
- (c) The Parameter Convergence is Universal (Independent of the Particular Physical System).
- (d) The Relative Scale of Successive Branch Splittings is Universal (Independent of the Particular Physical System).

Figure 22. Examples of Bifurcation Trees



(a) Point Attractor: A Damped Harmonic Oscillator-model of a Pendulum.
 (b) Limit-cycle Attractor: A Van der Pol Oscillator-model of a circuit Oscillator.

Figure 23. Examples of Attractors

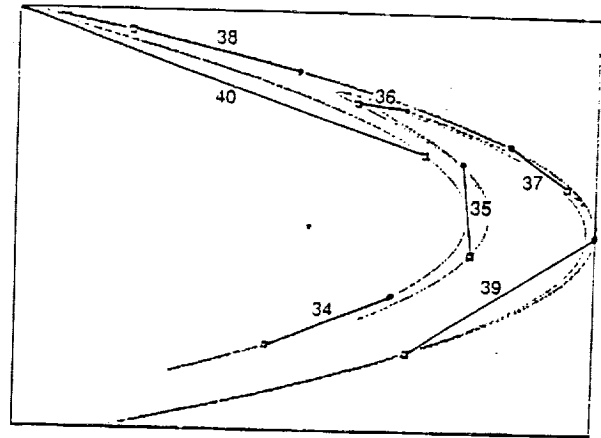


Figure 24. Example of a Strange Attractor

Attractors that can show chaotic behavior represent exponential sensitivity to initial conditions. Consider two initial conditions $|f_1>_0$ and $|f_2>_0 = |f_1>_0 + |\epsilon>_0$. The dynamical evolution gives a final state $|f_1>_t$ and $|f_2>_t$, as shown in Figure 25.

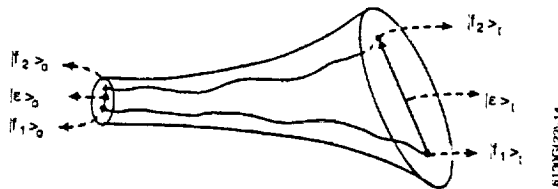


Figure 25. Exponential Evolution of Two Near Orbits in Phase Space

After time t , the distance between the two orbits is $|\epsilon>_t = |f_2>_t - |f_1>_t$. In the limit $|\epsilon>_0 \rightarrow 0$ and $t \rightarrow \text{large}$, orbits remain bounded and the difference between the solutions $|\epsilon>_t$ evolve exponentially for a

given direction of $|\epsilon>_0$. That is, $\left| \frac{|\epsilon>_t}{|\epsilon>_0} \right| \sim e^{\lambda t}$, $\lambda > 0$. Therefore, the system is very sensitive to initial conditions and is chaotic. This means that small errors in the prediction can evolve rapidly with time. Thus, there is a time horizon at which noise and computer roundoff can totally change the dynamics. To illustrate this computational limit, a computer experiment is performed on a simple attractor of Figure 24, with $A = 1.4$ and $B = 0.3$.

As shown in Figure 24, we have generated 34 to 40 iterates of an orbit starting from an identical initial condition $|f_1>_0 = 0$, $|f_2>_0 = 0$. The computations are identical except that one uses single precision and the other double precision. Single-precision round-off error is 10^{-14} . Single precision is indicated by squares and double precision by circles. For every iterate connected with a vector, we see that at the 40th iteration, the magnitude of this vector is as large as the variables themselves. Consequently, if using a computer that has 10^{-14} round-off error, prediction after the 40th iteration is nothing but a guess if the dynamics we are working with are indeed chaotic and have a Hénon attractor. This was just an example. In practice, the chaotic attractor of a solar flux time series should be identified before any meaningful prediction procedure is implemented, which is the goal of such an approach to solar flux prediction.

Returning to the Hénon map example, we see that after the first iterate, $|\epsilon_{>_1}$ and $|\epsilon_{>_0}$ are different by an order of 10^{-14} (round off). If in the next iteration, the error doubles ($e^{\ln 2t} = 2^t$), then the $|\epsilon_{>_1}$ and $|\epsilon_{>_0}$ are different by an order of attractor size in $t = 45$ ($2^t 10^{-14} = 1$). That is, if the error doubles, it is impossible to improve prediction. If we want to predict the evolution past $t = 45$ to $t = 90$, which is twice as long a prediction; then we should have an accuracy of 10^{-28} , which is 14 orders of magnitude more accurate. Therefore, improving prediction by a factor of two is impossible.

In other words, structural stability (Topological Orbital Equivalence [TOE]) breaks over a time horizon, making prediction impossible. Therefore, structural stability and computability are inherently incompatible. This is precisely why weather prediction over a time horizon is impossible. Lorenz' conclusion for weather-generating mechanisms was that thermally driven convections could make the atmosphere chaotic.

Now, returning to our problem, we have many reasons to believe that multiple interactions in the Sun introduce nuclear, chemical, electrodynamic, hydrodynamic, and other nonlinearities. It is easy to visualize chaotic behavior in solar flux because the Sun is like a rotating fluid that introduces turbulence, and its sunspots are similar to convection rolls. These behaviors introduce chaos just as does the Rayleigh-Benard mechanism. Furthermore, all atmospheres are really chaotic—even those ionized gases in solar atmosphere that chaotically modulate solar radio emission.

4. CONCLUSIONS

In May of 1990, we postulated that solar flux is a chaotic time series. This postulation was apparent from many physical features of the Sun. For example, the Sun is a rotating fluid that introduces turbulence, and most of the interactions, whether chemical, nuclear, or other, are nonlinear. We have also argued that the pattern in the logarithm of the power spectrum and the autocorrelation function is a concrete example that solar flux is a pattern-structured, time series. Therefore, an approach to study solar flux should be through nonlinear chaotic dynamics.

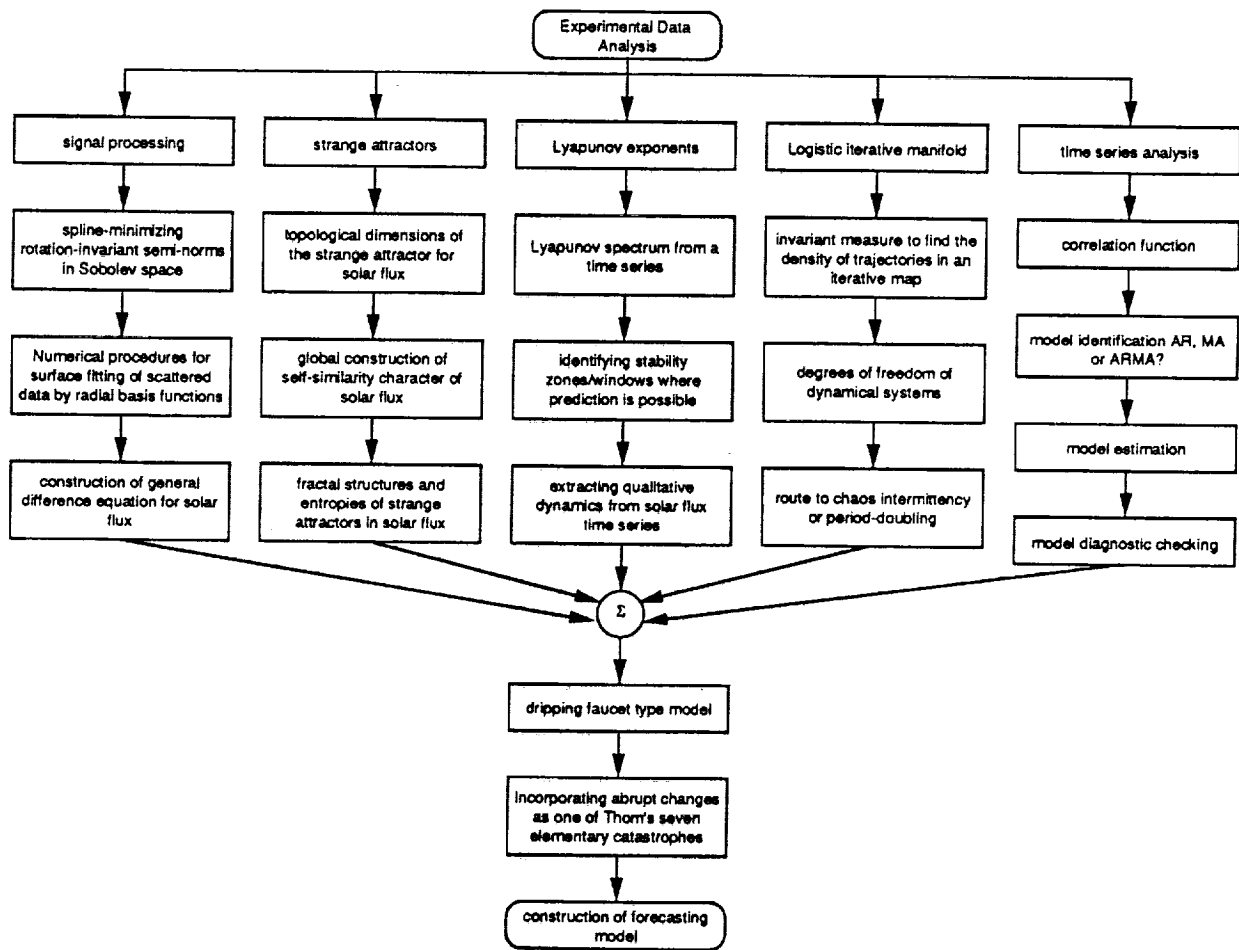
We have further claimed that a time horizon exists above which predictions are computationally impossible. To demonstrate this claim, we used the dripping faucet attractor, which roughly resembles the multiple periodicities observed in the dynamics of the solar flux. We also suggested that the Hénon-type attractors provide good candidates for study, although in the absence of a detailed demonstration that strange attractors or ensembles of strange attractors are really Hénon types, this theory remains in the realm of speculation.

Convection rolls were also introduced as models of sunspots that are products of nonlinear interaction (like solitons). These convection rolls could be produced in the ionized gases of solar atmosphere, further modulating (chaotically) the solar flux signal.

We also discovered evidence of a period-doubling type of route to chaos in the behavior of solar flux. In this case, we observed less power at frequencies that follow the well-known period-doubling bifurcations. This was further recognized as a new form of order that could be a new route to chaos. We also found evidence of fractal (self-similarity invariance, under contraction and dilation) structure in solar flux that deserves a separate investigation (see Figure 26).

ACKNOWLEDGMENTS

Thanks to D. Ashrafi, C. Schiff, M. Rokni, and In-Hwan Oh for valuable discussions, suggestions, and support. It is also a pleasure to thank J. Yorke for his suggestion to use cascaded linear maps to reconstruct our time series; C. Grebogi for proper directions; and E. Ott for teaching the fundamental concepts of chaos.



61305(22)-09

Figure 26. Future Investigation Possibilities

REFERENCES

1. P. McIntosh, "Did Sunspot Maximum Occur in 1989?" *Sky & Telescope*, 1991
2. In-Hwan Oh, "The Average Solar Flux (F10.7 cm) Model For an 11-Year Solar Cycle," prepared for NASA GSFC (contract # NAS-11933 mod 13) by Wolf Research and Development Corp., September 1974
3. J. C. Brandt, *Introduction to Solar Wind*, W. Freeman & Company, 1970
4. J. Cappellari, A. Long, C. Velez, and A. Fuchs, *Goddard Trajectory Determination System (GTDS)*, CSC/TR-89/6021, prepared for NASA GSFC (Contract NAS 5-31500) by Computer Sciences Corporation, July 1989
5. S. Ashrafi, *Future Mission Studies on Preliminary Comparisons of Solar Flux Models*, FDD/554-91/004, prepared for NASA GSFC (contract NAS 5-31500), by Computer Sciences Corporation, December 1990
6. S. Ashrafi, *Future Mission Studies on Solar Flux Analysis*, FDD/554-91/006, prepared for NASA GSFC (contract NAS 5-31500) by Computer Sciences Corporation, December 1990
7. S. Ashrafi, "Existence of a Time Horizon for 'Structural Stability' and 'Computability' to Become Formally Incompatible in Prediction of Solar Flux," (In Preparation)
8. S. Ashrafi, "Toward Modeling the Formation of Abrupt Changes in Solar Flux by Thom's Catastrophe Theory," (In Preparation)
9. E. A. Jackson, *Perspectives of Nonlinear Dynamics*, Cambridge University Press, 1989
10. G. Box and G. Jenkins, *Time Series Analysis*, Holden-Day, 1976
11. P. Cvitanovic', *Universality in Chaos*, Bristol, England: Adam Higler, 1984
12. "Predictability in Science and Society," *Proceedings of a Joint Symposium of the Royal Society and the British Academy*, 1986
13. R. Cahalan, H. Leidecker, and G. Cahalan, "Chaotic Rhythms of a Dripping Faucet," *Computers in Physics*, August 1990
14. E. Ott, "Chaos in Dynamical Systems," (preprint) 1991

